Journal of Catalysis 271 (2010) 186–194

Contents lists available at ScienceDirect

Journal of Catalysis

journal homepage: www.elsevier.com/locate/jcat

Methanol-to-olefin conversion over H-MCM-22 and H-ITQ-2 zeolites

Hyung-Ki Min, Min Bum Park, Suk Bong Hong *

Department of Chemical Engineering and School of Environmental Science and Engineering, POSTECH, Pohang 790-784, Republic of Korea

ARTICLE INFO

Article history:
Received 16 November 2009
Revised 8 January 2010
Accepted 9 January 2010
Available online 2 February 2010

Keywords:
MTO
MCM-22 and ITQ-2
Pore architecture
Acidity
Product selectivities and deactivation stability

ABSTRACT

The methanol-to-olefin (MTO) performance of H-MCM-22 and H-ITQ-2, as well as of their dealuminated analog prepared via oxalic acid treatment, is compared with the catalytic behavior of H-ZSM-5 and H-SAPO-34. The contribution of two-dimensional sinusoidal 10-ring channels in H-MCM-22 to the overall catalytic action of this medium-pore zeolite, especially to the propene selectivity, was found to be considerably greater than that of its cylindrical supercages, probably due to the smaller void volume and hence to the higher concentration of intrazeolitic reactant molecules. Despite the much larger cage volume (480 vs. 240 Å^3), H-MCM-22 shows a much slower deactivation rate than H-SAPO-34. A similar result, although less pronounced, can be observed when compared to the channel-based H-ZSM-5 zeolite with a slightly lower Si/Al ratio (14). The overall results of our study demonstrate that not only the pore architecture (cage-based vs. channel-based pore systems) of zeolitic materials but also the properties (density, strength, and location) of their acid sites are a critical factor governing the MTO selectivity and stability.

1. Introduction

From both scientific and industrial viewpoints, methanol-to-olefin (MTO) conversion on microporous solid acids such as zeolites and silicoaluminophosphate (SAPO) molecular sieves has been one of the most important issues in the field of heterogeneous catalysis over the past several decades [1,2]. Up to date, more than 20 distinct reaction mechanisms, which can be broadly divided into direct (consecutive) and indirect (parallel) routes, have been proposed to elucidate the MTO chemistry. Although the first C–C bond formation in the kinetic induction period of the MTO process is still a matter of debate, there is a general consensus that the post-induction time reaction observed for cage-based, small-pore materials like H-SAPO-34 (framework type CHA) proceeds through the so-called hydrocarbon pool mechanism [2]. The essential feature of this indirect route is that organic reaction centers act as scaffolds for producing light olefins (i.e., ethene and propene) within the pores of molecular sieves so as to get away from the high-energy intermediates required by all direct mechanisms. Moreover, the hydrocarbon pool mechanism is a space-demanding process involving a number of cyclic organic intermediates. Thus, the actual catalytic cycle can differ notably according to the pore topology of zeolitic solids employed [3,4]. For example, hexamethylbenzene and heptamethylbenzenium cation have been identified as main hydrocarbon pool species on H-SAPO-34 with 20-hedral *cha*-cages (6.7 Å in diameter and 10.0 Å in height) interconnected by 8-ring (3.8 × 3.8 Å) windows and H-beta (*BEA) with mutually perpendicular 12-ring (5.6 × 5.6 and 6.6 × 6.7 Å) channels, respectively [5,6].

MCM-22 (MWW) is among the most interesting zeolite structures in that it contains two independent pore systems: one formed by two-dimensional sinusoidal 10-ring (4.1 × 5.1 Å) channels and the other by large cylindrical supercages (7.1 Å in diameter and 18.2 Å in height) that can be accessible only through 10-ring (4.0 × 5.5 Å) windows [7]. Fig. 1 shows the projection of the MCM-22 framework down the *c*-axis, together with schematic drawings of its intralayer sinusoidal channel and interlayer large supercage systems [8,9]. The lack of direct connection between each of the channel- and cage-based pore systems has led us to consider the proton form (H-MCM-22) of this medium-pore zeolite as a suitable system of better understanding the role of the pore architecture of microporous solids acids on the MTO activity and selectivity. To date, however, there is little known on the catalytic properties of H-MCM-22 for this reaction.

In the present study, we compare the catalytic performance of H-MCM-22 and its delaminated material (i.e., H-ITQ-2), which does not contain large cylindrical supercages [10], with that of H-SAPO-34 and H-ZSM-5 (MFI), the two most widely studied and best MTO catalysts. The acidic properties of H-MCM-22 and H-ITQ-2 were found to be notably different from those of the latter two materials. Hence, the catalytic results presented here could also illustrate the effects of the acidity of zeolites and related materials on their MTO activity and deactivation behavior. On the other hand, most of the external surface of MCM-22 and ITQ-2 crystallites, which typically appear as very thin plates, is terminated by 12-ring cups or pockets

* Corresponding author. Fax: +82 54 2798299.
E-mail address: sbhong@postech.ac.kr (S.B. Hong).

0021-9517/$ - see front matter © 2010 Elsevier Inc. All rights reserved.
doi:10.1016/j.jcat.2010.01.012

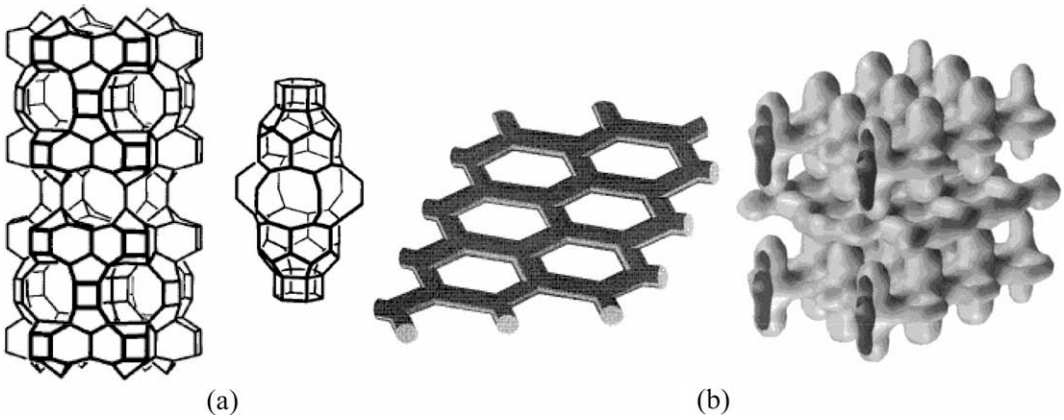

Fig. 1. (a) Skeletal drawings of the MWW framework showing two double layers (left) and the large cylindrical supercage (right). (b) Schematic drawings of the intralayer sinusoidal channels (left) and of both large cavities and channels (right) in MCM-22. Adopted from Refs. [8,9], respectively.

(7.1 Å in diameter and 7.0 Å in depth) with fully connected tetrahedral atoms (T-atoms). Thus, Al atoms located in their external 12-ring pockets give rise to strong acid sites on the surface that are similar to the internal Brønsted acid sites of zeolites. This has also led us to compare the catalytic properties of H-MCM-22 and H-ITQ-2 before and after oxalic acid treatment in order to elucidate the effects of zeolitic external acid sites on the MTO selectivity and stability.

2. Experimental

2.1. Catalyst preparation

An MCM-22 zeolite with a Si/Al ratio of 16.8 was synthesized using hexamethyleneimine as an organic structure-directing agent according to the procedures described elsewhere [11]. A portion of the crystallized product, frequently denoted MCM-22(P), was calcined in air at 550 °C for 8 h, giving MCM-22, and then converted to its proton form by refluxing twice in 1.0 M NH_4NO_3 solutions (0.03 g mL^{-1}) for 6 h, followed by calcination at 550 °C for 4 h. Another portion of MCM-22(P) was delaminated in accordance with the procedures developed by Corma et al. [10,12], to prepare the ITQ-2 sample. Dealumination was carried out by refluxing H-MCM-22 and H-ITQ-2 in 1.0 M oxalic acid solutions (0.02 g mL^{-1}) for 24 h. After acid treatment, zeolite particles were filtered off and washed first with cold and then hot distilled water until all traces of remaining acid removed. The dealuminated H-MCM-22 and H-ITQ-2 zeolites are referred to as H-MCM-22(D) and H-ITQ-2(D), respectively. For comparison, two H-ZSM-5 zeolites with Si/Al = 14 and 140 were obtained from Tosoh and Zeolyst and denoted H-ZSM-5(I) and H-ZSM-5(II), respectively. In addition, H-SAPO-34 (Si/Al = 0.12) with an average crystal size of 2–6 μm was synthesized according to the Exxon patent [13].

2.2. Characterization

Powder X-ray diffraction (XRD) patterns were measured on a PANalytical X'pert diffractometer (Cu Kα radiation) with an X'Celerator detector. Elemental analysis was carried out by the Analytical Laboratory of the Korea Institute of Science and Technology. The Si/Al ratios in the superficial region of zeolite crystals were determined by X-ray photoelectron spectroscopy (XPS) with a VG ESCALAB 220iXL spectrometer employing an Mg K_α X-ray source (1253.6 eV). Typically, 20 scans were accumulated and all the binding energies are referenced to the C(1*s*) line at 284.6 eV from adventitious carbon. Then, the superficial Si/Al ratios were calculated from the Si(2*p*) and Al(2*p*) line intensities using appropriate sensitivity factors. N_2 sorption experiments were performed on a Mirae SI nanoPorosity-XG analyzer. Acidic properties of the catalysts were determined by temperature-programmed desorption (TPD) of NH_3. The TPD measurements were carried out on a home-made TPD instrument equipped with a thermal conductivity detector (TCD). Before adsorption of NH_3, a sample of ca. 0.1 g was activated in flowing He (50 cm^3 min^{-1}) at 550 °C for 2 h. Then, 10 wt.% NH_3 was pulsed to the sample at 150 °C for 0.5 h and subsequently purged with He at the same temperature for 1 h to remove the physisorbed NH_3. The TPD was obtained in flowing He (30 cm^3 min^{-1}) from 150 to 650 °C with a ramping rate of 10 °C min^{-1}. The ^{27}Al MAS NMR spectra at a spinning rate of 5.0 kHz were recorded on a Varian Inova 300 spectrometer at a ^{27}Al frequency of 78.156 MHz with a $\pi/8$ rad pulse length of 1.8 μs and a recycle delay of 0.5 s. Typically, ca. 1000 pulse transients were accumulated. The ^{27}Al chemical shifts are reported relative to an $Al(H_2O)_6^{3+}$ solution.

Thermogravimetric analyses (TGA) were performed in air on an EXSTAR 6000 thermal analyzer, where the weight loss related to the combustion of coke deposits formed during MTO was further confirmed by differential thermal analyses (DTA) using the same analyzer. The coke species formed on the catalysts after MTO at 400 °C for different periods of time on stream were also characterized by gas chromatography–mass spectroscopy (GC–MS). The coke materials were extracted by the following method developed by Guisnet and Magnoux [14]. To examine changes in the relative concentrations of the organics formed in zeolitic pores with time on stream, the exactly same amount (50 mg) of the used catalyst was always dissolved in 3 mL of 10% HF solution. After neutralization with K_2CO_3, CCl_4 (Aldrich, 99.5%) was employed to extract the organic species from the resulting solution. A small amount of Na_2SO_4 was added to remove the residual water in the organic phase and then recovered using an Advantec DISMIC-13JP syringe filter. The GC–MS total ion chromatograms of extracted organic phases were recorded on a Varian CP-3800 gas chromatograph equipped with a Varian 320-MSD mass selective detector, using electron impact ionization at 70 eV. The split ratio was 100:1, and the column used was a VF-5 capillary column (30 m × 0.25 mm) with flowing He (0.3 cm^3 min^{-1}). The temperature program ramps the column from 70 to 280 °C at a rate of 4 °C min^{-1}. The on-column experiments were done under these conditions, using the specific injector. The organic compounds extracted were identified in comparison with the NIST database [15].

2.3. Catalysis

MTO was carried out under atmospheric pressure in a continuous-flow apparatus with a fixed-bed microreactor. Prior to the experiments, the catalyst was routinely activated under flowing N_2 (130 $cm^3\ min^{-1}$) at 550 °C for 2 h and kept at 400 °C to establish a standard operating procedure, allowing time for the reactant/carrier gas distribution to be stabilized. Then, methanol (MeOH) vapor was fed at a rate of 0.5 $cm^3\ h^{-1}$ (4.0 h^{-1} WHSV) into the reactor containing 0.1 g of catalyst at the same temperature. The total gas flow at the reactor inlet was kept constant at 30 $cm^3\ min^{-1}$. When necessary, the WHSV was adjusted from 4.0 to 20.0 h^{-1}, by increasing the temperature of a MeOH saturator. The reaction products were analyzed on-line in a Varian CP-3800 gas chromatograph equipped with a CP-PoraPLOT Q capillary column (25 m × 0.25 mm) and a flame ionization detector, with the first analysis carried out after 5 min on stream. CO_2 was separated using a Carbosphere packed column and analyzed with a TCD. The column temperature was maintained at 70 °C for 1 min and then increased to 180 °C at a ramping rate of 10 °C min^{-1}. Conversion was defined as the percentage of MeOH consumed during the MTO reaction, and dimethylether was not considered as a product. The yield of each product was calculated as the percentage to the amount (in mole) of MeOH converted to hydrocarbons.

Flushing experiments, in which the MeOH-containing stream was replaced by a pure N_2 stream (30 $cm^3\ min^{-1}$), were also performed as a function of time at 400 °C. Each flushed sample was subjected to the same HF dissolution procedure as described previously, to follow the evolution of the organic compounds accumulated within their inner pores with increasing flushing time. When necessary, MeOH was again reacted over the flushed catalyst at 400 °C and 4.0 h^{-1} WHSV.

3. Results and discussion

Fig. 2 shows the powder XRD patterns of H-MCM-22, H-ITQ-2, and their dealuminated analogs prepared via oxalic acid treatment. The positions and relative intensities of all the X-ray peaks from these materials are in good agreement with those reported in the literature [10,12,16]. The lack of (0 0 1) and (0 0 2) reflections at $2\theta = 3–7°$ in the XRD patterns of H-ITQ-2 and H-ITQ-2(D) indicates a significant reduction of long-range order along the *c*-axis during the delamination process.

The physical properties of the zeolitic catalysts studied in this work are listed in Table 1. While no significant increase in bulk Si/Al ratio of H-MCM-22 is caused by oxalic acid treatment, this is not the case of its Si/Al ratio in the superficial region determined by XPS to a depth of ~50 Å. In fact, it has been repeatedly shown that oxalic acid treatment can remove the surface/near-surface Al atoms of medium-pore zeolites more selectively than Al in the internal channels or cavities without causing serious structural collapse [17,18]. As seen in Table 1, however, H-ITQ-2 shows a significant increase in both bulk and superficial Si/Al ratios after oxalic acid treatment, mainly due to its delaminated nature that can be further supported by its very high external surface area (670 $m^2\ g^{-1}$).

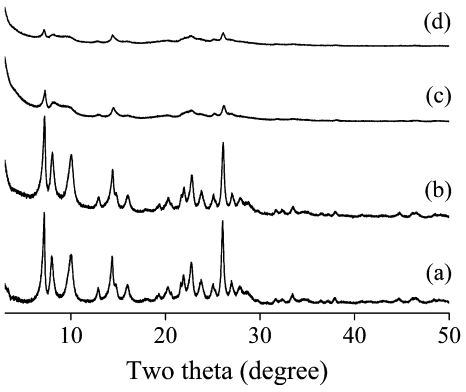

Fig. 2. Powder XRD patterns of (a) H-MCM-22, (b) H-MCM-22(D), (c) H-ITQ-2, and (d) H-ITQ-2(D) prepared in this study.

Fig. 3 shows the NH_3 TPD profiles from all zeolitic catalysts employed here. The TPD profiles from both H-MCM-22 and H-MCM-22(D) are characterized by two desorption peaks with maxima in the temperature regions 250–260 and 390–400 °C assigned to NH_3 desorption from weak and strong acid sites, respectively. As seen in Fig. 3, however, the total area of NH_3 desorption (i.e., the density of acid sites), especially the area of the low-temperature peak, is considerably smaller for the latter zeolite than for the former one. This suggests that the distribution of weak acid sites in H-MCM-22 is higher on the external 12-ring pockets than on the intracrystalline void spaces, because those sites can be more selectively removed during oxalic acid treatment. A quite similar conclusion was also drawn from the TPD curves of H-ITQ-2 and H-ITQ-2(D), although the densities of their acid sites are lower than those of H-MCM-22 and H-MCM-22(D), respectively, as expected from the composition data in Table 1. It is worth noting here that the strong acid sites in H-SAPO-34 and H-ZSM-5(I) have considerably higher density and strength than those in the other five materials, while a broader strength distribution is observed for the latter zeolite. In particular, the density of acid sites in H-ZSM-5(I) with a bulk Si/Al ratio of 14 is almost twice as large as that in H-MCM-22 or H-ITQ-2 characterized by a slightly higher Si/Al ratio (17 or 19). This can be partly rationalized by considering that the amount of residual Na^+ ions is considerably smaller in H-ZSM-5(I) than in the latter two materials (Table 1). An additional explanation is that the extent of dealumination occurred during the calcinations and ion exchange steps to prepare the proton form may be less severe in H-ZSM-5(I) than in H-MCM-22 or H-ITQ-2. In fact, ^{27}Al MAS NMR experiments have revealed that a fairly lower fraction of octahedral Al is observed for H-ZSM-5(I) (Fig. S1).

Fig. 4 shows MeOH conversion and selectivities to ethene ($C_2^=$) and propene ($C_3^=$) as a function of time on stream (TOS) in the MTO reaction over H-MCM-22, H-ITQ-2, H-ZSM-5(I), H-ZSM-5(II), and H-SAPO-34 measured at 400 °C and 4.0 h^{-1} WHSV. It can be seen that all five catalysts exhibit initial MeOH conversions of 100% or so, but their deactivation patterns and selectivities to $C_2^=$ and $C_3^=$ are quite different from one another. Although the cage-based, small-pore H-SAPO-34 material with the highest density of strong acid sites among the molecular sieves studied here (Fig. 3) gives the highest selectivity to light olefins (i.e., $C_2^= + C_3^=$) at the beginning of the reaction, for example, it is fully deactivated within 2 h on stream. By contrast, the channel-based, medium-pore H-ZSM-5(II) zeolite with the highest Si/Al ratio of 140, and hence with the lowest density of acid sites, is characterized by conversions around 95% during the period of 40 h on stream, together with the highest $C_3^=$ selectivity (ca. 43%). We also note that despite the presence of cylindrical supercages in H-MCM-22 whose volume (480 $Å^3$) is twice as large as that (240 $Å^3$) of *cha*-cages in H-SAPO-34, this medium-pore zeolite with Si/Al = 17 exhibits much better stability. Although modest, this is even true when compared to H-ZSM-5(I) with a slightly lower Si/Al ratio of 14. Of particular interest is the occurrence of an induction period for $C_3^=$ formation over H-MCM-22, but not for $C_2^=$ formation. During the first 1 h on stream, as seen in Fig. 4, the $C_3^=$ selectivity rapidly increases and then levels off while conversions around 100% remain constant, implying the generation of new catalytically active sites in H-MCM-22 at early TOS. Fig. 4 also shows that the practically super-

Table 1
Physical properties of zeolitic catalysts prepared in this study.

Catalyst	IZA code	Si/Al ratio		Residual Na^+ content[a] (wt.%[c])	Crystal shape and size[d] (μm)	BET surface area[e] ($m^2\ g^{-1}$)		
		Bulk[a]	Surface[b]			Total	External	Microporous
H-MCM-22	MWW	16.8	17.7	0.07	Thin plates, 0.1 × 1.0	460	100	360
H-MCM-22(D)		17.3	21.9	0.08		450	50	400
H-ITQ-2	–	19.2	20.3	0.08	Thin plates, 0.01 × 1.0	730	670	60
H-ITQ-2(D)		30	42	0.08		590	540	50
H-ZSM-5(I)	MFI	14.0	14.2	<0.02	Ellipsoids, 0.3 × 1.0	380	110	270
H-ZSM-5(II)		140	125	<0.02	Spheroids, 1.5 × 1.5 × 1.0	420	60	360
H-SAPO-34	CHA	0.12	0.22	–[f]	Cuboids, 2.0–6.0	530	10	520

[a] Determined by elemental analysis.
[b] Determined by XPS.
[c] Anhydrous basis.
[d] Determined by SEM.
[e] Calculated from N_2 adsorption data.
[f] Not determined.

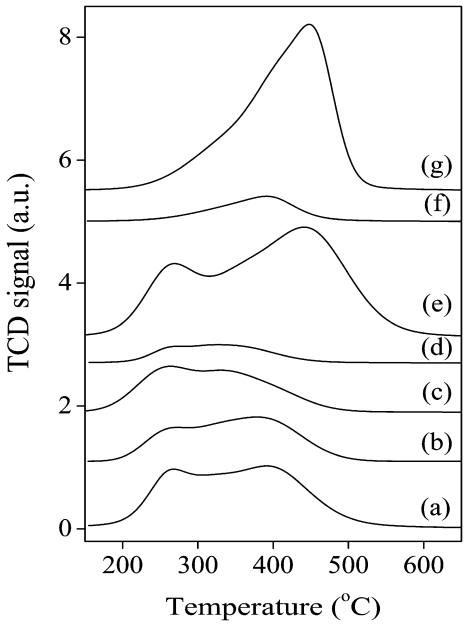

Fig. 3. NH_3 TPD profiles from (a) H-MCM-22, (b) H-MCM-22(D), (c) H-ITQ-2, (d) H-ITQ-2(D), (e) H-ZSM-5(I), (f) H-ZSM-5(II), and (g) H-SAPO-34.

cage-free H-ITQ-2 zeolite shows a rapid decrease in MeOH conversion at early TOS, but recovers its original value after ca. 10 h on stream, which will be further discussed later. Coupled with the NH_3 TPD results in Fig. 3, therefore, it is clear that the MTO activity and selectivity of zeolitic catalysts can be notably altered according not only to the geometrical constraints imposed by the particular pore structure of each material, but also to their acidic properties.

Fig. 5 shows MeOH conversion and selectivities to $C_2^=$ and $C_3^=$ as a function of TOS in MTO over H-MCM-22(D) and H-ITQ-2(D) measured under the reaction conditions described previously. H-MCM-22(D) exhibits a slight decrease in MeOH conversion during the period of 40 h on stream. Thus, this dealuminated zeolite has better MTO stability than its parent material, i.e., H-MCM-22. We also note that H-MCM-22(D) exhibits a considerably higher initial $C_3^=$ selectivity (28% vs. 20%), but shows a quite similar induction period in $C_3^=$ formation to that found in H-MCM-22. As seen in Fig. 5, as a result, its $C_3^=$ selectivity jumps up to 44% within 1 h on stream, which becomes comparable to the value of H-ZSM-5(II), and then slightly decreases over the rest of the period of TOS studied. On the other hand, H-ITQ-2(D) shows a notable decrease in MeOH conversion at early TOS. This is essentially identical to the trend observed for H-ITQ-2, but no recovery of conversion with prolonged TOS was found. The chemical composition data in Table 1 indicate that the superficial Si/Al ratio (42) of H-ITQ-2(D) is approximately twice as large as the ratio (20) of H-ITQ-2. It thus appears that the acid sites located in the external 12-ring pockets

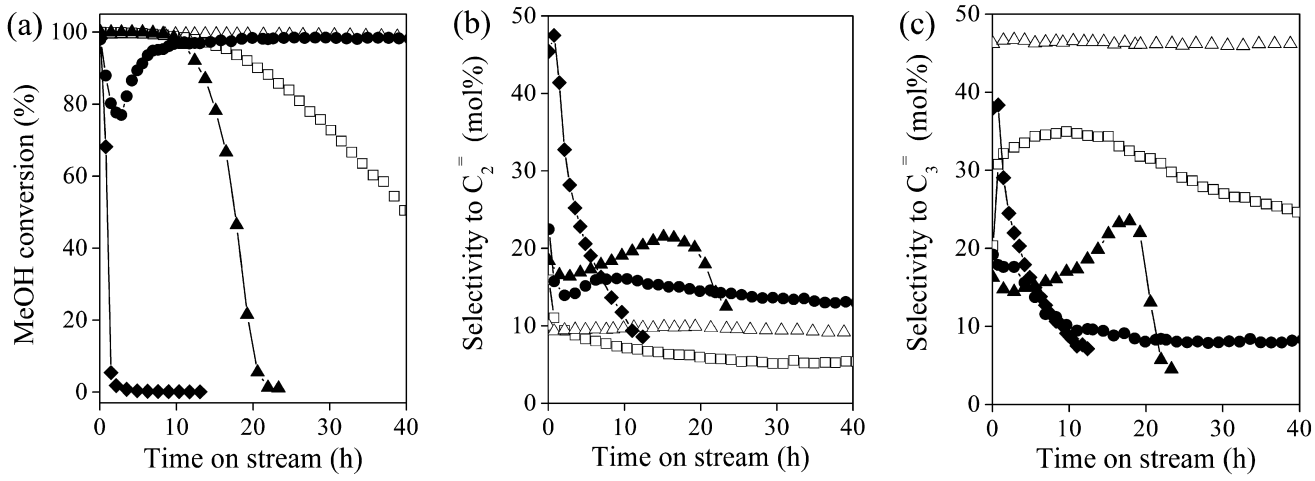

Fig. 4. (a) Methanol conversion and selectivities to (b) ethene and (c) propene as a function of time on stream in MTO reaction over H-MCM-22 (□), H-ITQ-2 (●), H-ZSM-5(I) (▲), H-ZSM-5(II) (Δ), and H-SAPO-34 (♦) at 400 °C and 4.0 h^{-1} WHSV.

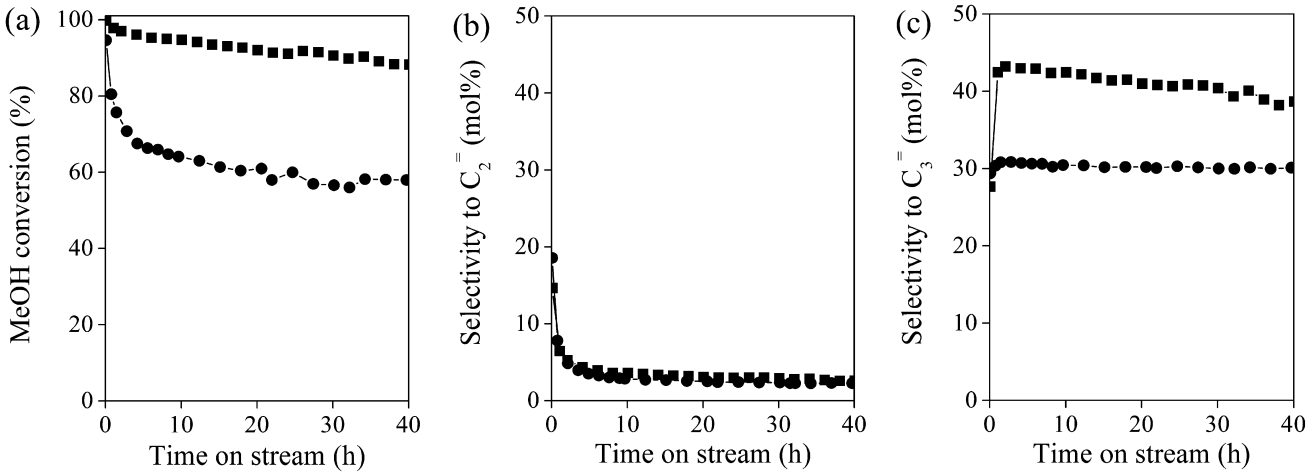

Fig. 5. (a) Methanol conversion and selectivities to (b) ethene and (c) propene as a function of time on stream in MTO over H-MCM-22(D) (■) and H-ITQ-2(D) (●). The reaction conditions are the same as those given in Fig. 4.

are associated with the recovery of MeOH conversion observed for H-ITQ-2 (Fig. 4).

Another interesting observation obtained from Fig. 5 is that the initial $C_3^=$ selectivity (28%) of H-ITQ-2(D), within which large supercages are hardly preserved, is nearly the same as the value (29%) of H-MCM-22(D) and remains almost constant during the period of 40 h on stream. This implies that the $C_3^=$ formation over both H-MCM-22(D) and H-ITQ-2(D) at the beginning of the reaction occurs mainly within their sinusoidal 10-ring channels. In particular, the fact that the observed increase (14%) in $C_3^=$ selectivity over H-MCM-22(D) during the induction period is barely half the initial selectivity (28%), which strongly suggests that the contribution of sinusoidal 10-ring channels in H-MCM-22(D), as well as in its parent zeolite, to the $C_3^=$ formation is much greater than that of cylindrical supercages, within which MTO catalysis after some TOS is dominated by the hydrocarbon pool mechanism. It thus appears that the channel-based material may be more effective for achieving higher MeOH conversion and $C_3^=$ selectivity than the cage-based one, probably due to the smaller void volume and hence to the higher concentration of intrazeolitic reactant molecules, once they have the same largest ring (e.g., 10-ring) limiting access to the pore system.

Table 2 lists the conversions and product distributions from MTO over a series of molecular sieve catalysts with different pore structures and/or compositions measured at 400 °C and 4 h^{-1} WHSV after 5 min and 10 h on stream. These data reveal that butanes (mainly isobutane) are one of the major products observed for H-MCM-22, H-ITQ-2, and H-ZSM-5(I) at the beginning of the reaction, while the other four catalysts produce a much larger amount of $C_2^=$ or $C_3^=$. Table 2 also shows that among the seven zeolitic materials, H-ITQ-2 is the only one characterized by the simultaneous decrease and increase in selectivities to $C_3^=$ and methane (C_1) after 10 h on stream, respectively. It has long been suggested that C_1 formation over H-ZSM-5 during MTO may occur via direct methylation of the coke deposits on the catalyst with MeOH followed by C_1 elimination, unlike the case of other higher alkanes [19]. This stimulated us to focus our interest on changes in the C_1 selectivity of H-ITQ-2 in line with TOS and then to compare the results with those obtained from the three related materials, i.e., H-MCM-22, H-MCM-22(D), and H-ITQ-2(D). As seen in Fig. 6, H-ITQ-2 exhibits a continuous increase in C_1 selectivity during the first 15 h on stream. Then, its selectivity levels off into ca. 20% over the rest of the period of TOS studied. After a small decrease at early TOS, however, the C_1 selectivity of both H-MCM-22(D) and H-ITQ-2(D) levels off into a steady state. A similar trend can also be observed for H-MCM-22, although there is a slight increase in C_1 selectivity after ca. 15 h on stream.

The characterization results in Table 1 indicate that the external surface area of H-ITQ-2 is much larger than the area of H-MCM-22 or H-MCM-22(D). Thus, the number of external acid sites should be

Table 2
Conversion and product distribution from MTO over various zeolitic catalysts at 400 °C and 4.0 h^{-1} WHSV.

Catalyst	TOS (h)	MeOH conversion (%)	Selectivity (mol.%)									
			C_1	C_2	C_3	C_4	C_5+C_6	$C_2^=$	$C_3^=$	$C_2^=+C_3^=$	$C_4^=$	Aromatics
H-MCM-22	0.083	100	5.1	0.5	7.4	26.6	17.3	15.9	20.3	36.2	4.6	2.2
	10	99	2.3	0.1	1.7	9.5	27.7	7.1	34.7	42.0	9.3	7.6
H-MCM-22(D)	0.083	100	4.5	0.4	4.8	17.4	16.9	15.1	30.6	45.7	8.1	2.1
	10	94	1.2	0.1	1.1	6.3	26.5	4.4	43.3	47.7	12.6	4.5
H-ITQ-2	0.083	98	5.1	0.6	3.5	19.3	21.1	22.5	19.2	41.7	5.3	2.6
	10	97	18.3	1.0	2.3	22.3	24.1	16.1	9.8	25.9	2.4	3.9
H-ITQ-2(D)	0.083	95	3.5	0.4	2.9	11.3	21.6	18.6	29.4	48.0	10.2	2.2
	10	64	2.5	0.1	0.6	7.7	30.6	2.9	30.5	33.4	14.7	10.5
H-ZSM-5(I)	0.083	100	3.9	1.1	19.58.9	23.8	8.1	18.4	16.3	34.7	5.3	3.4
	10	98	6.6	0.5		18.0	9.9	19.1	17.0	36.1	4.7	15.5
H-ZSM-5(II)	0.083	97	0.7	0.1	1.6	10.4	15.3	10.4	44.8	55.2	14.7	2.1
	10	97	0.8	0.1	1.7	10.5	14.2	11.4	42.3	53.7	14.0	5.0
H-SAPO-34	0.083	98	2.3	0.5	2.7	6.0	1.7	45.4	38.0	83.4	3.5	0
	10	~0										

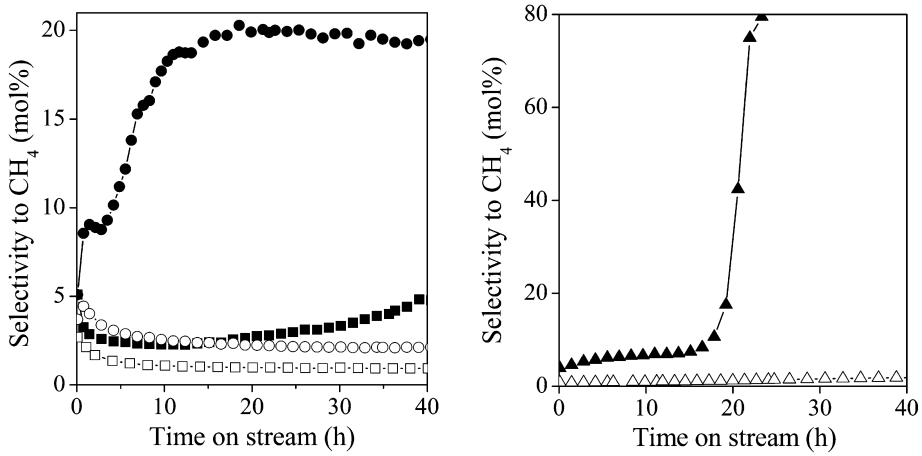

Fig. 6. Selectivity to methane as a function of time on stream in MTO over H-MCM-22 (■), H-MCM-22(D) (□), H-ITQ-2 (●), H-ITQ-2(D) (○) H-ZSM-5(I) (▲), and H-ZSM-5(II) (Δ). The reaction conditions are the same as those given in Fig. 4.

much larger in the former zeolite. A similar conclusion can also be drawn from comparison with H-ITQ-2(D), due to the much lower superficial Si/Al ratio (20 vs. 42) of H-ITQ-2. This suggests that the main location of catalytically active sites responsible for C_1 formation during MTO over H-ITQ-2 may be its external 12-ring pockets. If such were the case, the rapid decrease in MeOH conversion observed at early TOS for this delaminated zeolite (Fig. 4) should then be attributed to the formation of large coke precursor molecules on the external 12-ring pockets, rendering the acid sites inaccessible for catalysis. Once coke precursors are converted to real coke, however, MeOH is directly reacted with coke to produce C_1 via the initial methylation and the subsequent cracking [19], resulting in the recovery of its conversion to the original value as seen in Fig. 4. Because the initial coke formation over H-MCM-22 occurs mainly within its large supercages, on the other hand, direct methylation of coke with MeOH for C_1 production over this medium-pore zeolite should be more sterically hindered compared with the same reaction over the essentially supercage-free H-ITQ-2 material. Also, if coke deposition starts to occur mainly on the external 12-ring pockets of H-MCM-22 after some TOS, the slight increase in its C_1 selectivity observed after ca. 15 h on stream could then be explained. Due to the low density of acid sites in their external surface, by contrast, H-MCM-22(D) and H-ITQ-2(D) appear to give no further changes in the C_1 selectivity even after 5 h on stream.

Fig. 6 also shows C_1 selectivity as a function of TOS in MTO over H-ZSM-5(I) and H-ZSM-5(II). The C_1 selectivities of both H-ZSM-5(I) and H-ZSM-5(II) are low at the beginning of the reaction. The selectivity of latter zeolite with a low Al content (Si/Al = 140) remains unchanged during the period of 40 h on stream, which correlates well with its excellent $C_3^=$ selectivity and MTO stability. As seen in Fig. 6, however, H-ZSM-5(I) with a high Al content (Si/Al = 14), which begins to rapidly deactivate after ca. 20 h on stream (Fig. 4), exhibits a sudden increase in C_1 selectivity at a similar TOS. We should note here that oxalic acid treatment of H-ZSM-5(I) gives rise to a notable increase in its MTO stability (Fig. S2). Therefore, it is clear that pore blockage instead of intrazeolitic active site coverage by coke deposition on the external surface of zeolite crystallites during MTO may be the main origin of deactivation of channel-based, medium-pore materials like H-ZSM-5, as repeatedly suggested [20,21]. Then, C_1 selectivity can be regarded as a useful measure of investigating catalyst deactivation in this reaction.

The catalytic results in Figs. 4 and 5 have revealed that the dealuminated analog of both H-MCM-22 and H-ITQ-2 has comparable MTO stability to that of H-ZSM-5(II), despite the higher Al contents. In fact, no significant decrease in MeOH conversion over these three zeolites was found even after 72 h on stream at 400 °C and 4.0 h^{-1} WHSV. To further compare their stabilities, therefore, we have carried out MTO over H-MCM-22(D), H-ITQ-2(D), and H-ZSM-5(II) as a function of TOS at the same temperature but at a much higher WHSV of 20.0 h^{-1}. As seen in Fig. 7, H-ZSM-5(II) is much more active than the former two catalysts over the period of TOS studied. We also note that the practically supercage-free H-ITQ-2(D) zeolite again shows a considerably high rate of deactivation at early TOS compared to H-MCM-22(D). Because the density and strength of acid sites are fairly lower and weaker in the former material, respectively (Fig. 3), the poor MTO activity and stability observed for this delaminated, dealuminated zeolite can be attributed to its very large external surface area.

Fig. 8 shows coke formation as a function of TOS over all seven catalysts in MTO at 400 °C and 4.0 h^{-1} WHSV. Coupled with the NH_3 TPD results in Fig. 3, it is clear that the rate of coke formation on zeolites and molecular sieves during MTO can notably vary not only with the pore topology of the material employed, but also with its acidic properties, as previously reported [1,22]. For example, the rate of coke formation at early TOS is higher on the cage-containing H-SAPO-34 and H-MCM-22 materials than on the channel-based H-ITQ-2 and H-ZSM-5(I) zeolites. This indicates the internal buildup of coke in the former two materials at the beginning of the reaction. In line with its rapid deactivation (Fig. 4), in particular, the rate of coke formation is much faster on H-SAPO-34 than on any of the other materials studied here, which may be attributed to the synergy of its strong acidity and cage-based structure. Fig. 8 also shows that while H-MCM-22 and H-ITQ-2 give a continuous increase in coke content even after 24 h on stream, coke formation over H-MCM-22(D) and H-ITQ-2(D) almost levels off after this TOS. Therefore, the main location for coke formation on these zeolites after some TOS appears to be their external 12-ring pockets. A quite similar conclusion can be obtained from H-ZSM-5(I) with a comparable density of strong acid sites to that of H-SAPO-34 (Fig. 3).

Large organic compounds, generally termed coke, formed via hydrocarbon conversions end up entrapped inside the void spaces of the acid zeolite catalysts employed. Hence, the characterization of coke deposited on MTO catalysts has provided valuable information not only on the reaction intermediates yielding light olefins but also on the aromatic hydrocarbon species responsible for catalyst deactivation [2,23]. Because the free diameter (5.8 Å) at the intersection of the two sinusoidal 10-ring channels retained in

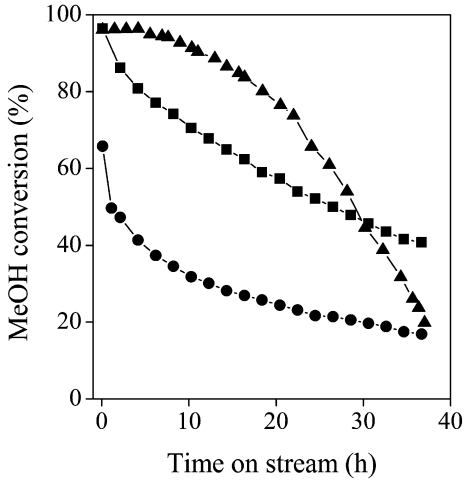

Fig. 7. Methanol conversion as a function of time on stream in MTO over H-MCM-22(D) (■), H-ITQ-2(D) (●), and H-ZSM-5(II) (▲) at 400 °C and 20.0 h^{-1} WHSV.

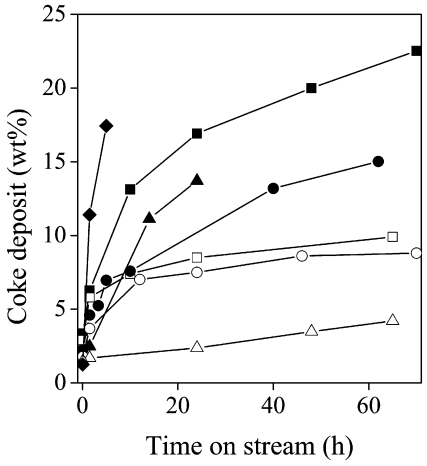

Fig. 8. Coke formation as a function of time on stream in MTO over H-MCM-22 (■), H-MCM-22(D) (□), H-ITQ-2 (●), H-ITQ-2(D) (○), H-ZSM-5(I) (▲), H-ZSM-5(II) (△), and H-SAPO-34 (♦) at 400 °C and 4.0 h^{-1} WHSV.

both MCM-22 and ITQ-2 is even smaller than the diameter (6.2 Å) at the intersection of the straight and sinusoidal 10-ring channels in ZSM-5, it is not difficult to expect that the formation of active reaction centers at early TOS in MWW-type zeolites occurs mainly within their large supercages. As described previously, in addition, the external acid sites on the H-MCM-22 and H-ITQ-2 crystallites have a harmful effect on their MTO activities and selectivities. To identify the hydrocarbon pool species responsible for the formation of light olefins within the supercages of the MWW structure, therefore, we carried out GC–MS analyses of a series of H-MCM-22(D) catalysts after MTO at 400 °C and 4.0 h^{-1} WHSV for different periods of TOS.

Fig. 9 shows the GC–MS total ion chromatograms of the CCl_4 extracts of this series of used H-MCM-22(D) catalysts, together with the assignments of the observed peaks made by comparing their mass spectra with the NIST database [15]. The major aromatic hydrocarbon compounds formed after 90 min on stream are polymethylbenzenes with 2–5 methyl groups, naphthalene, and methylnaphthalenes, while hexamethylbenzene is barely detectable. However, we note that the amounts of naphthalene and methylnaphthalenes continuously increase with increasing TOS. The same trend can also be observed for acenaphthene and 1*H*-phenalen-1-one whose signals begin to appear after 24 h on

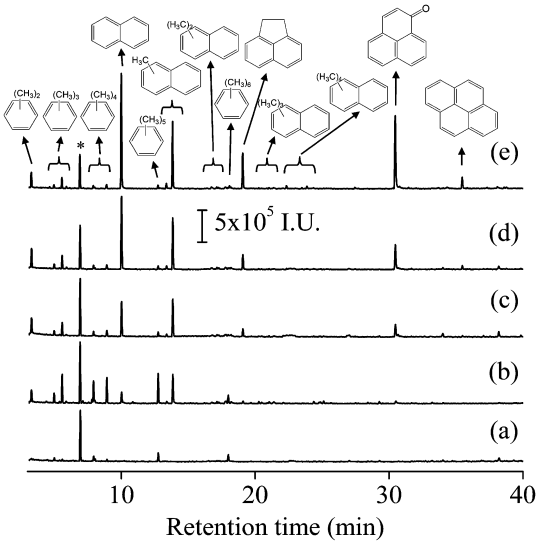

Fig. 9. GC–MS total ion chromatograms of the CCl_4 extracts of H-MCM-22(D) after MTO at 400 °C and 4 h^{-1} WHSV for (a) 0.083, (b) 1.5, (c) 12, (d) 24, and (e) 72 h on stream. The structures annotated onto the chromatograms are peak identifications in comparison with the mass spectra to those in the NIST database [15], and the asterisk represents the mass signal of C_2Cl_6 produced by the pyrolysis of CCl_4 at the GC injection temperature (300 °C).

stream, when H-MCM-22(D) remains active (Fig. 5). It thus appears that these di- and tricyclic aromatic compounds may be associated with the deactivation of H-MCM-22(D) in the end, although this dealuminated zeolite is not severely deactivated even after 72 h on stream. Here, we speculate that 1*H*-phenalen-1-one, the only one oxygen-containing species among the organic compounds given in Fig. 9, has been formed from some C_{13} precursor, most likely 1*H*-phenalene, during HF dissolution, as is the case with acetophenone identified by the GC–MS analysis of LaNa-Y (FAU) after ethylbenzene disproportionation at 130 °C for 30 h on stream [24]. By contrast, tetra- and pentamethylbenzenes exhibit a notable decrease in intensity after 12 h on stream, which is not the case of di- and trimethylbenzenes. This suggests that the former two higher methylbenzenes are the main hydrocarbon pool species for the formation of olefins inside the supercages of H-MCM-22(D), which can be further supported by the much higher selectivity of this dealuminated zeolite to $C_3^=$ over $C_2^=$ (Fig. 5). In fact, the number of methyl groups in methyl-substituted benzene rings has been shown to regulate the type of light olefins formed: $C_2^=$ is predominantly formed from the lower methylbenzenes, whereas $C_3^=$ formation is highly favored by methylbenzenes with 4–6 methyl groups [21,25].

It is interesting to note that the hydrocarbon species retained in H-MCM-22(D) are quite similar to those not only in H-MCM-22, but also in H-ITQ-2(D) (Fig. S3). This implies that the selective accumulation of polycyclic aromatic compounds such as acenaphthene and 1*H*-phenalene in the structurally well-defined external 12-ring pockets of H-MCM-22 and H-ITQ-2 is also possible. Indeed, the molecular widths (6.8–6.9 Å) of acenaphthene and 1*H*-phenalene calculated using Chem 3D Ultra version 9.0 (CyberChem) are marginally smaller than the diameter (7.0 Å) of their external 12-ring pocket. Since the same result can be obtained in comparison with the molecular lengths (ca. 6.8 Å) of naphthalene and methylnaphthalenes, the empty supercages and/or external 12-ring pockets in the MWW structure appear to act as reverse templates for the formation of these polyaromatics during MTO, like the selective accumulation of methylpyrenes within the 22-hedral cages of the SAPO molecular sieve STA-7 (SAV) [26]. We should note here that phenanthrene and pyrene with molecular widths of 5.6 and

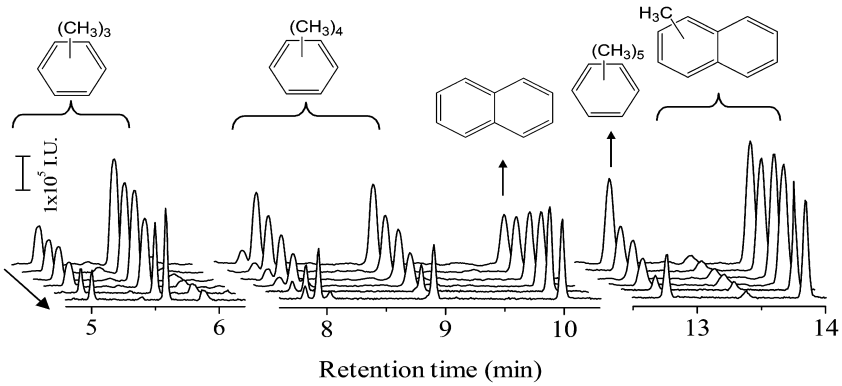

Fig. 10. GC–MS total ion chromatograms of the CCl_4 extracts of H-MCM-22(D) after MTO at 400 °C and 4.0 h^{-1} WHSV for 90 min followed by flushing with N_2 at the same temperature for (from rear to front) 0, 2, 4, 8, and 32 min and then by reacting with methanol for 10 min.

6.9 Å, respectively, are the two most dominant compounds found in the fully deactivated H-SAPO-34 catalyst containing *cha*-cages of 7.5 Å in diameter and 8.1 Å in length (Fig. S4), which is consistent with the previous GC–MS study by Fu et al. [27]. Given the notable difference in the NH_3 TPD profiles of H-MCM-22 and H-SAPO-34 (Fig. 4), it is clear that the type of aromatic hydrocarbon species leading to deactivation can differ according to the acidic properties of zeolitic catalysts, as well as to their pore topology.

To further clarify the role of tetra- and pentamethylbenzenes as organic reaction centers, exactly the same amount (0.1 g) of H-MCM-22(D) was reacted with MeOH at 400 °C for 90 min on stream and then flushed in a pure N_2 stream at the same reaction temperature for different times. The GC–MS chromatograms of the CCl_4 extract of this series of flushed catalysts are shown in Fig. 10. For simplicity, only the regions representing polymethylbenzenes with 3–5 methyl groups, naphthalene, and methylnaphthalenes are presented. It can be seen that the tetra- and pentamethylbenzene signals notably decrease with increasing flushing time, revealing their instability at 400 °C. As seen in Fig. 10, however, trimethylbenzenes give a much smaller decrease in intensity, which is also the case of naphthalene and methylnaphthalenes. This can be rationalized by suggesting that a non-negligible amount of trimethylbenzenes together with light olefins are generated by the decomposition of higher methylbenzenes upon flushing [28]. When the flushed H-MCM-22(D) catalyst for 32 min was again reacted with MeOH for 10 min, on the other hand, a more notable increase in intensity is observed for tetra- and pentamethylbenzenes. Therefore, we can conclude that these two polymethylbenzene species are actual organic reaction centers dominating the catalytic action of supercages in MWW-type zeolites.

Taking into account the catalytic and characterization results presented thus far, several guiding principles for the development of more stable MTO catalysts than the already known ones can be established. First and quite simply, it is essential to minimize the number of external acid sites on the molecular sieve crystallites via various post-synthetic methods known to date [29], because MTO catalysis over such acid sites is hardly shape-selective. Second, the MTO performance of H-ITQ-2 and H-ITQ-2(D) suggests that the zeolitic materials had better not have a very large external surface area. Therefore, we suspect that the decrease in their crystallite size from the microscale to the nanoscale range (e.g., the $\leqslant$50 nm range) in which the relative proportion of T-atoms at the external surface to those inside the crystallites is no longer negligible, giving a notably small microporosity compared to microcrystalline materials [30], could have a harmful effect on the MTO selectivity and stability. Further study is currently underway in our laboratory to confirm this possibility. Third, the relatively high MTO stability observed for H-MCM-22(D) suggests that more careful control of the strength of acid sites in cage-based materials is necessary to retard the intrazeolitic formation of polyaromatic hydrocarbons that make them rapidly deactivated. Fourth, the discovery of new multi-dimensional 10-ring materials with pore dimensions slightly smaller than those of ZSM-5 is highly desirable, because certainly improved MTO stability compared to the already known channel-based, medium-pore zeolites is expected.

4. Conclusions

MTO has been investigated not only over H-MCM-22 and H-ITQ-2, but also over their dealuminated analog prepared via oxalic acid treatment, at 400 °C and atmospheric pressure in order to elucidate the relative importance of cage-based vs. channel-based structures of zeolitic catalysts and of external vs. internal acid sites on the catalytic properties for this reaction. It was found that the contribution of supercages to the overall MTO performance of H-MCM-22 is considerably smaller than that of its sinusoidal channels. Also, the acid sites located in the external 12-ring pockets of H-MCM-22 and H-ITQ-2 crystallites proved to be detrimental to the MTO selectivity and stability. MTO catalysis in their sinusoidal 10-ring channels is dominated by methylation-cracking reactions that selectively produce propene rather than ethene as a primary product. However, the catalytic action of the cage-based pore system in H-MCM-22 is governed by the hydrocarbon pool mechanism, although it is also selective to propene formation. GC–MS analyses reveal that tetra- and pentamethylbenzenes are organic reaction centers dominating the catalytic performance of supercages in H-MCM-22, which explains the high propene selectivity observed for this medium-pore zeolite. On the basis of the overall results of our study, some useful propositions for developing more stable MTO catalysts are presented.

Acknowledgments

This work was supported by the Korea Science and Engineering Foundation through the National Research Laboratory Program (R0A-2007-000-20050-0) and SK Energy. We thank Prof. J.M. Park (POSTECH) for access to his GC–MS facilities.

Appendix A. Supplementary material

Supplementary data associated with this article can be found, in the online version, at doi:10.1016/j.jcat.2010.01.012.

References

[1] M. Stöker, Microporous Mesoporous Mater. 29 (1999) 3.
[2] J.F. Haw, W. Song, D.M. Marcus, J.B. Nicholas, Acc. Chem. Res. 36 (2003) 317.
[3] W. Song, J.F. Haw, J.B. Nicholas, C.S. Heneghan, J. Am. Chem. Soc. 122 (2000) 10726.
[4] M. Bjørgen, U. Olsbye, D. Petersen, S. Kolboe, J. Catal. 221 (2004) 1.
[5] B. Arstad, S. Kolboe, J. Am. Chem. Soc. 123 (2001) 8137.
[6] A. Sassi, M.A. Wildman, H.J. Ahn, P. Prasad, J.B. Nicholas, J.F. Haw, J. Phys. Chem. B 106 (2002) 2294.
[7] M.E. Leonowicz, J.A. Lawton, S.L. Lawton, M.K. Rubin, Science 264 (1994) 1910.
[8] M.A. Camblor, A. Corma, M.-J. Diaz-Cabanas, Ch. Baerlocher, J. Phys. Chem. B 102 (1998) 44.
[9] S.L. Lawton, M.E. Leonowicz, R.D. Partridge, P. Chu, M.K. Rubin, Microporous Mesoporous Mater. 23 (1998) 109.
[10] A. Corma, V. Fornes, S.B. Pergher, Th.L.M. Maesen, J.G. Guglass, Nature 396 (1998) 353.
[11] A. Corma, C. Corell, J. Perez-Pariente, Zeolites 15 (1995) 655.
[12] A. Corma, V. Fornes, J. Martinez-Triguero, S.B. Pergher, J. Catal. 186 (1999) 57.
[13] M. Mertens, K.G. Stromaier, US Patent 6,773,688, 2004.
[14] M. Guisnet, P. Magnoux, Appl. Catal. 54 (1989) 1.
[15] S.E. Stein, NIST Mass Spec Data Center, in: P.J. Linstrom, W.G. Mallard (Eds.), NIST Chemistry WebBook, NIST Standard Reference Database No. 69, National Institute of Standards and Technology, Gaithersburg, MD, 2005.
[16] H.J. Jung, S.S. Park, C.-H. Shin, Y.-K. Park, S.B. Hong, J. Catal. 245 (2007) 65.
[17] M.R. Apelian, A.S. Fung, G.J. Kenndy, T.F. Degan, J. Phys. Chem. 100 (1996) 156577.
[18] S.-H. Lee, C.-H. Shin, S.B. Hong, J. Catal. 223 (2004) 200.
[19] H. Schulz, W. Böhringer, W. Baumgärtner, S. Zhao, Stud. Surf. Sci. Catal. 28 (1986) 915.
[20] H.G. Karge, E.P. Boldingh, Catal. Today 3 (1988) 53.
[21] M. Bjørgen, S. Svelle, F. Joensen, J. Nerlov, S. Kolboe, F. Bonino, L. Palumbo, S. Bordiga, U. Olsbye, J. Catal. 249 (2007) 195.
[22] H.G. Karge, Stud. Surf. Sci. Catal. 137 (2001) 707.
[23] M. Guisnet, J. Mol. Catal. A 182–183 (2002) 367.
[24] H.-K. Min, V. Chidambaram, S.B. Hong, J. Phys. Chem. C 114 (2010) 1190.
[25] W. Song, H. Fu, J.F. Haw, J. Am. Chem. Soc. 123 (2001) 4749.
[26] M. Castro, S.J. Warrender, P.A. Wright, D. Apperley, Y. Belmabkhout, G. Pirnberger, H.-K. Min, M.B. Park, S.B. Hong, J. Phys. Chem. C 113 (2009) 15731.
[27] H. Fu, W. Song, J.F. Haw, Catal. Lett. 76 (2001) 89.
[28] B.P.C. Hereijgers, F. Bleken, M.H. Nilsen, S. Svelle, K.-P. Lillerud, M. Bjørgen, B.M. Weckhuysen, U. Olsbye, J. Catal. 264 (2009) 77.
[29] R. Szostak, Stud. Surf. Sci. Catal. 137 (2001) 261.
[30] M.A. Camblor, A. Corma, S. Valencia, Microporous Mesoporous Mater. 25 (1998) 59.